Manuscript Accepted by ACS Applied Materials & Interfaces

Proton Conducting Silicon Oxide Membranes as a Fluorine free Alternative to Nafion for Low Temperature Water Electrolysis

Jingjing Jin[a], Lucas A. Cohen[a], Sahand Adibnia[a], Alex Z. Lee[a], Kyungmin Yim[a], Matthew S. Weimer[b], Arrelaine A. Dameron[b], Sara Harris[b], Zhexi Lin[a], and Daniel V. Esposito[a,*]

[a]Columbia University in the City of New York

Department of Chemical Engineering

Columbia Electrochemical Energy Center

Lenfest Center for Sustainable Energy

New York, NY 10027, United States

[b]Forge Nano, Inc.

Thornton, CO 80241, United States

(*)Corresponding author

de2300@columbia.edu

ph. 212-854-2648

Abstract

Driven by environmental and health concerns related to per- and polyfluoroalkyl substances (PFAS), there has been growing interest in developing fluorine-free proton (H^+) exchange membrane (PEM) materials for fuel cells and water electrolyzers. In this study, we present a side-by-side comparison of the key transport properties of sub-micron thick, PFAS-free amorphous silicon dioxide (SiO_2) membranes to Nafion™, a fluorinated polymer electrolyte membrane that represents the industry standard for PEM fuel cells and electrolyzers. Measurements of proton (H^+) conductivity (σ_{H^+}), hydrogen (H_2) permeability (P_{H_2}), and electrical resistivity (ρ_{e^-}) were conducted using model thin films comprised of SiO_2 membranes deposited by atomic layer deposition (ALD). Although the H^+ conductivity of the SiO_2 membranes is 2-3 orders of magnitude lower than Nafion, the addition of phosphorous dopants (PO_x) improves H^+ conductivity such that the area specific membrane resistance of thin (< 50 nm) PO_x-doped SiO_2 membranes is more than an order of magnitude lower than Nafion-117. Importantly, the safe operation of such nanoscale membranes within a PEM electrolyzer is feasible thanks to the low H_2 permeability of dense SiO_2-based membranes, which are predicted to limit H_2 crossover rates to acceptable levels for pressures up to ≈ 100 bar. As a proof-of-principle demonstration, a chip-scale water electrolyzer based on 100 nm thick PO_x-SiO_2 membrane is shown to achieve a current density of 2 A cm^{-2} at a potential of 2.5 V. If this technology can be successfully scaled up, H^+ conducting oxide membranes offer an attractive PFAS-free alternative to Nafion for efficient and durable water electrolysis and fuel cell technologies.

Keywords: water electrolysis, fuel cells, PEM electrolyzer, hydrogen, membranes, proton conducting oxide membranes, silicon dioxide, Nafion, atomic layer deposition

I. Introduction

Hydrogen (H_2) is expected to be a key fuel and chemical building block in a clean energy future due to its high energy content and versatility across a wide range of applications.[1] Water electrolysis powered by renewable energy is one of the most promising methods to produce clean hydrogen without generating CO_2 emissions.[2] Proton exchange membrane (PEM) electrolyzers are a particularly promising electrolyzer technology due to their ability to achieve high efficiencies and high current densities, which are enabled by their "zero-gap" membrane electrode assembly (MEA) design wherein an ion exchange membrane is sandwiched between the cathode and anode catalyst layers (Figure 1a).[3] Membrane thicknesses in PEM electrolyzer typically range from 100 to 200 μm, which are significantly less than the separation distance between electrodes in conventional liquid alkaline electrolyzers (1.5 mm – 15 mm).[4, 5]

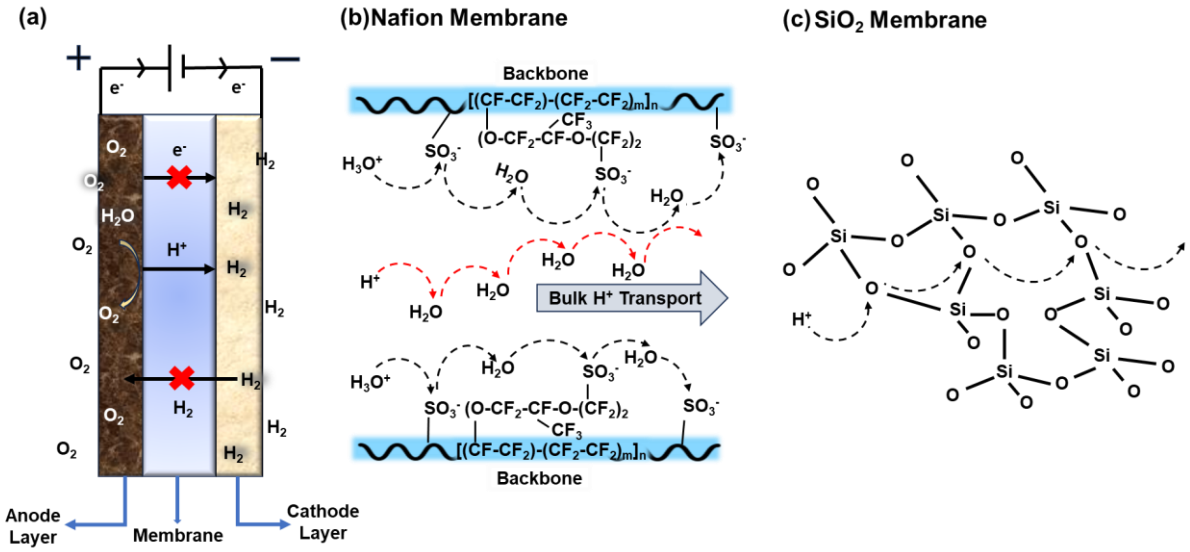

Figure 1. (a) Side view schematic of a PEM electrolyzer highlighting species transport processes. (b) Schematic of proton transport within a hydrated nanoscopic pore of a Nafion membrane, where the black arrows show H^+ transport by H^+ hopping along the surface of the channel walls and the red arrow shows bulk transport of H^+ hopping through the H-bond network of water. (c) Schematic of proton transport in SiO_2 membranes involving H^+ hopping by facilitated diffusion involving bridging oxygen atoms within the SiO_2 matrix.

Thanks to the shorter distance for ion transport in zero-gap cell designs, PEM electrolyzers have lower ohmic resistances that allow them to operate at relatively high efficiencies (65%–85% with respect to the lower heating value of H_2) at high current densities (1.5–3 $A \cdot cm^{-2}$).[6] The industry-standard membrane for PEM electrolyzers is Nafion™, a polymeric ion exchange membrane with a fluorinated backbone and sulfonate ion exchange groups (Figure 1b). Despite the commercial success of Nafion in both PEM electrolyzers and fuel cells, this polymeric membrane material has several shortcomings. Most notably, Nafion is a PFAS material, raising environmental and health concerns if fluorinated compounds – whether from spent or degraded membranes, or as byproducts of manufacturing – are released into the environment.[7] From a technical standpoint, there is also strong motivation to find alternatives to Nafion that allow for even lower membrane resistance without compromising safety. Despite having a very low area specific resistance (R_m) compared to liquid alkaline cells, the ohmic drop associated with H^+ transport across the Nafion membrane in a PEM electrolyzer still represents the largest overpotential loss in PEM electrolyzers at current densities over ≈ 2 A cm^{-2}.[8] Thus, developing new membranes with lower R_m than Nafion-117 presents an opportunity to enable next-generation PEM electrolyzers and fuel cells with even higher efficiencies and higher current densities. Technoeconomic analysis has shown that such gains in efficiency and current density resulting from reduced membrane resistance can translate into significant decreases in the levelized cost of H_2.[9]

One of the most straightforward paths to reducing R_m is to use thinner Nafion.[10, 11] For example, researchers have shown that using Nafion NR–211, which has a thickness of 25 μm, allows for reducing R_m down to 10.9 $m\Omega \cdot cm^2$ at 80 °C, subsequently enabling significant improvement in electrolyzer efficiency.[12] However, there are limits to decreasing the thickness of

Nafion much lower than ≈ 50 μm owing to changes in the mechanical properties of Nafion. Thinner Nafion membranes become more susceptible to tears and defects, causing significant challenges in stack assembly, while changes to the orientation and microstructure of hydrated channels within Nafion lead to decreases in the intrinsic H^+ conductivity.[10, 11] Another major challenge with using Nafion membranes with thicknesses thinner than 50 μm is the elevated rate of H_2 crossover, which can lead to unsafe mixtures of H_2 and O_2 on the anode side due to the higher flux of H_2 across the porous Nafion membrane. This issue becomes especially acute for PEM electrolyzers, where it is often desirable to operate with an elevated pressure of H_2 (>15 atm) on the cathode side to compress the H_2 product. Unfortunately, this pressure differential between the cathode and anode creates a large driving force for H_2 to diffuse across the membrane, which can readily occur in many polymeric membranes like Nafion thanks to fast diffusion through their high density of hydrated nanoscopic pores (see Figure 1b).[13] Recognizing the critical importance of balancing H^+ and H_2 transport, it is necessary to explore membrane materials that maximize the ratio of H^+ conductivity (σ_{H^+}) to H_2 permeability (P_{H_2}).[9, 14]

To combat the shortcomings of conventional polymeric ion exchange membranes, some researchers have explored oxide-based membranes or composite membranes comprised of polymers and inorganic materials as alternatives. For example, researchers have developed Nafion/SiO_2 composite membranes that combine the advantageous properties of Nafion with silicon dioxide (SiO_2), an inorganic material recognized for its excellent chemical stability and low P_{H_2}.[15,16] Proton-conducting oxide membranes (POMs), primarily perovskite oxides, have been extensively investigated in recent years for intermediate-temperature (25–400 °C) electrolysis and fuel cell applications.[17] However, simple oxides like TiO_2 and SiO_2 have also attracted interest, including for low-temperature microfluidic fuel cells.[18] The low P_{H_2} of defect-free SiO_2 and other

H^+-conducting oxides is primarily due to their dense structure, in contrast to hydrated Nafion, which has a of ≈ 28%.[19] Another important distinction between SiO_2 and Nafion lies in their values of their Young's modulus. The Young's modulus of amorphous SiO_2 at room temperature is approximately 70 GPa,[20]whereas Nafion exhibits a much lower value of about 0.1 GPa.[21] A higher modulus indicates greater stiffness and resistance to deformation under applied stress, implying that SiO_2 membranes are less susceptible to creep or plastic deformation during prolonged operation. However, similar to other ceramic materials, SiO_2 is more brittle and can be prone to crack formation. Ceramic membranes are nevertheless widely employed in high-temperature solid oxide fuel cells and electrolyzers, demonstrating the feasibility of such materials in practical applications. Furthermore, recent work by Esposito's research group has shown that mechanical defects such as pinholes and cracks in SiO_2 membranes can be mitigated by depositing nanoscopic "plug" materials into the defects, thereby minimizing hydrogen crossover through these localized regions.[22] Additionally, oxide materials like SiO_2 can be more environmentally friendly than PFAS-based membranes like Nafion. Despite generally lacking a hydrated pore structure like Nafion, SiO_2 membranes can still support H^+ conduction in their dense oxide matrix through facilitated diffusion whereby H^+ can hop between neighboring Si-O-Si and Si-O sites that serve as carrier centers as a part of the H-bonding network within the material (Figure 1c).[18] A significant challenge is that the σ_{H^+} of many oxide materials at low temperatures ranges from 10^{-8} to 10^{-4} S·cm^{-1}, which is 3–7 orders of magnitude lower than that of Nafion.[17] However, with its high density, SiO_2 membranes can be orders of magnitude thinner than Nafion while maintaining low H_2 permeance. Furthermore, when SiO_2 is doped with phosphorus or sulfonic acid, its ionic conductivity improves significantly, exhibiting values three to four orders of magnitude higher than those of undoped SiO_2 films.[23, 24]

In the current study, SiO_2 membranes of varying thickness were deposited by atomic layer deposition (ALD) as thin films onto a platinum thin film electrode, which serve as a well-defined test platform for characterizing the membranes and quantifying their transport properties relevant to water electrolysis. These model SiO_2 membranes were used to quantify σ_{H^+}, P_{H_2}, and ρ_{e^-}. Through a direct comparison of the properties of SiO_2 membranes to those of Nafion, the potential for using sub-micron thick H^+ conducting SiO_2 membranes for low-temperature water electrolysis is assessed. Importantly, this work shows that SiO_2 membranes doped with phosphorous can achieve a ratio of σ_{H^+} to P_{H_2} that is 10 – 20 times greater than Nafion. If nanoscale SiO_2 membranes having these characteristics can be successfully integrated into large scale, zero-gap MEAs, the resulting proton-conducting oxide membrane (POM) electrolyzers can enable low temperature water electrolysis at significantly higher current densities and/or efficiencies than conventional Nafion-based PEM electrolyzers.

II. Materials and Methods

2.1 SiO_2 Membrane Synthesis

Electrodes were prepared from a monocrystalline, p-type silicon wafer (prime grade, p+Si (100), resistivity <0.005 Ω-cm, 500–550 μm thick, University Wafer). A 50 nm thick platinum (Pt) catalyst layer with a 2 nm Ti adhesion layer were electron-beam deposited onto the silicon wafer under high vacuum ($<6 \times 10^{-8}$ Torr) at a rate of 1 Å s^{-1}. SiO_2 membranes were deposited on top of the Pt catalyst by ALD, which was performed using a Forge Nano ALD^x APOLLO legacy reactor.[25] Upon introduction to the reactor, samples were held under 1000 sccm of N_2 for 60 seconds to reach thermal equilibrium, followed by a 30 second ozone (O_3) exposure to remove adventitious carbon contamination from the surface. The precursor was delivered via 6" showerhead utilizing 40 Torr N_2 as a carrier and purge gas. SiO_2 ALD was performed with

bis(ethylmethylamino)silane (BEMAS) heated to 45 °C in a vapor draw configuration as the Si precursor and a combination of O_3 mixed with a nitrogen-based catalyst, the catalyst is periodically entrained into the O_3 flow, as the conversion half-cycle.[26] The SiO_2 ALD dose scheme was 31 ms - 965 ms - 966 ms - 980 ms (BEMAS exposure - BEMAS purge - O_3/catalyst exposure - O_3/catalyst purge). The growth per cycle of this SiO_2 ALD process is ~1.39 Å/cy, so each 50 nm deposition received roughly 360 cycles. Phosphorus was incorporated into the SiO_2 ALD via an ABC type process with the addition of trimethyl phosphite $P(OMe)_3$.[27] In ABC-type ALD, a dopant precursor (component C) is introduced immediately after the oxidant or conversion step of the main ALD process (components A and B), enabling in-situ incorporation of dopant species within each ALD cycle. PO_x-SiO_2 had a deposition sequence of 31 ms - 965 ms - 966 ms - 980 ms - 250 ms - 4990 ms (BEMAS exposure - BEMAS purge - O_3/catalyst exposure - O_3/catalyst purge - $P(OMe)_3$ exposure - $P(OMe)_3$ purge). Addition of $P(OMe)_3$ to the process created a slight decrease in the amount of growth per cycle, down to 1.36 Å/cy, so each 50 nm deposition required 370 cycles.

2.2 Membrane Characterization

Thickness for undoped SiO_2 and PO_x-SiO_2 ALD films to calculate growth per cycles (GPC) were investigated using a spectroscopic ellipsometry (SE) at a fixed angle (75°). These raw ellipsometry data were modeled from cos(2Ψ) and sin(2Ψ) cos(Δ), measured from data generated using a dual light source over the range of 225-1000 nm (combined deuterium and halogen sources) and an Si-based array detector. Regression analysis was performed via the Levenberg–Marquardt fitting algorithm employing a dispersion method (Cauchy, Exponential, Sellmeier, and Tauc-Lorentz), and the model was fit over the wavelength range of 250 to 1000 nm. From these data and modeling procedures, thickness, refractive index (RI) at 633 nm, and extinction coefficient (k) at 633 nm were determined. To aid the fidelity of modeling, a thick film of >50 nm was deposited on Si

wafers. This thick film allows for greater confidence in thickness uniformity, as well as RI and k. Ellipsometry was also used to characterize films as deposited on an electrolysis test platform. Films deposited on the test vehicle were modelled using an infinite slab of Pt, ignoring the Si underneath and resulted in a goodness of fit > 0.97 for all data collected. Chip-scale water electrolyzer was made by spray painting IrO_x/C mixture on top of the ALD SiO_2/Pt electrode. X-ray photoelectron spectroscopy (XPS) measurements were done with a PHI XPS system at pressures $< 2 \times 10^{-10}$ torr using a monochromatic Al Kα source (15 kV, 20 mA) and a charge neutralizer, tilted to 54.7° relative to the detector. Surface topography and roughness was measured using a Bruker Dimension Icon atomic force microscope (AFM) in air using a ScanAsyst silicon tip on a nitride cantilever with a 2 nm nominal tip radius and a spring force constant of 0.4 N m^{-1}. Measurements were performed in peak force nanomechanical mapping mode using a scan rate of 0.22 Hz and a resonant frequency of 70 kHz. Zeiss Sigma VP field emission scanning electron microscopy (FE-SEM) with Schottky thermal field emission type electron gun was used to obtain high magnification images. Energy dispersive X-ray spectroscopy attachment (Bruker xFlash 6 | 30 Detector) of the FE-SEM instrument was used for elemental mapping and analysis. The wettability of the SiO_2 surfaces was evaluated using a Rame-Hart Model 260 goniometer under ambient conditions. Static water contact-angle measurements were performed using deionized water droplets. For each sample, measurements were taken at multiple locations across the surface, and the reported values represent the mean ± 95% confidence interval calculated from replicate measurements.

2.3 Transport Measurements

Electrochemical measurements were conducted using an SP-200 BioLogic potentiostat, a commercial Ag|AgCl (3.0 M KCl) reference electrode (E° = 0.21 V vs. NHE, Hach, E21M002), a

carbon rod counter electrode (Saturn Industries), and a rotating disk electrode (RDE) setup (PINE Research Instrumentation). Wafer electrodes were mounted to the RDE with a custom rotator attachment (2 in. diameter), which allowed the electrode to be mounted flush with the bottom of the shaft, and they were masked with electroplaters tape (3M) to expose a circular active area with diameter 0.38 cm. The electrolyte for all electrochemical experiments was deaerated by purging nitrogen (Airgas, 99.99% purity) for 20 minutes prior to experimentation. The total resistance of each electrode was measured by performing potentiometric electrochemical impedance spectroscopy (PEIS) at 0.096 V vs. RHE from 1 MHz to 1 Hz with an amplitude of 10 mV. Linear sweep voltammetry (LSV) for SiO_2/Pt-based electrodes was performed between 0 and 1.65 V vs. RHE with a scan rate of 20 $mV \cdot s^{-1}$ for five cycles to measure the limiting current density of the hydrogen oxidation reaction (HOR) at a rotation speed of 600 rpm. For electrical resistivity measurements, submicron-thick oxide membranes were strategically positioned between a 50 nm Pt catalyst layer and a layer of silver paint, secured in place with Cu tape on top and wrapped in electroplaters tape with electrode tabs exposed. Current-voltage (I-V) curve data were collected in a dry environment, where the measured resistance was used to calculate the electrical resistance of the membrane. The electrolyte temperature was controlled using a silicone oil bath (Ace Glass) and monitored with a liquid-in-glass thermometer (Grainger, FEP-coated glass). The Nafion-117 reference membrane used for hydrogen permeability measurements was soaked into 5% H_2O_2 at 80 °C for 1 and boiled in 0.5 M H_2SO_4 and deionized water for 1 hour each to remove impurities and ensure full protonation. After pretreatment, the Nafion-117 membrane was adhered to a Pt-coated Si wafer held in place using 3M electroplater's tape.

III. Results and discussion

3.1 Characterization of SiO_2 and PO_x-SiO_2 Membranes

Membranes fabricated by ALD were prepared under varying deposition temperatures, conditions, and levels of phosphorus incorporation. The thickness of each deposited layer was precisely controlled by adjusting the number of ALD cycles and quantitatively determined using spectroscopic ellipsometry, ensuring reliable and reproducible film growth across all samples. To further validate these measurements and assess film morphology, cross-sectional and top-view scanning electron microscope (SEM) imaging were conducted. The thicknesses of ALD SiO_2 membranes determined from cross-sectional SEM images showed excellent agreement with the thicknesses determined by ellipsometry. Representative SEM images and EDS characterization results are provided in the Supporting Information (Section I).

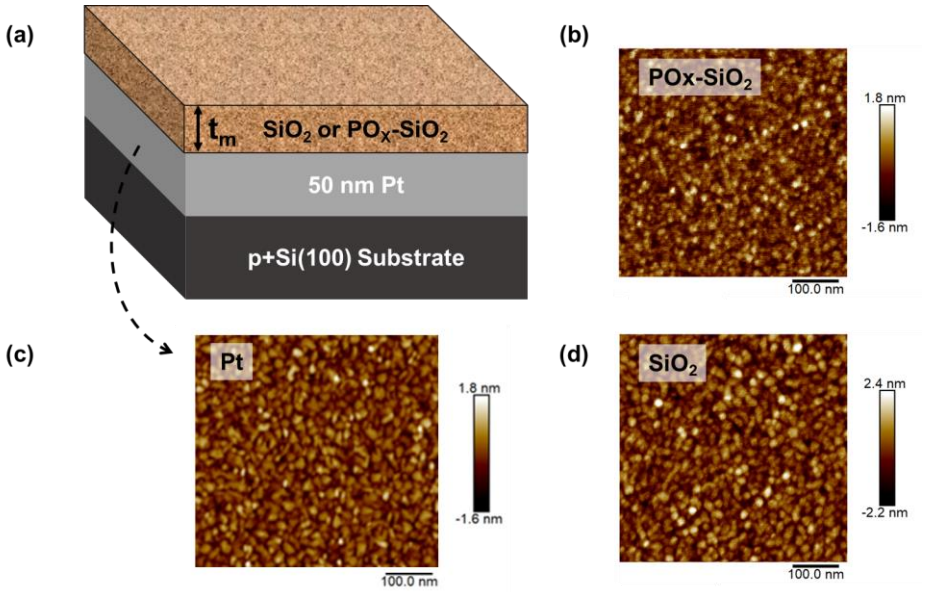

Figure 2. (a) Schematic of SiO_2-coated Pt thin film used for measuring H_2 permeability and H^+ conductivity. Representative AFM images of (b) 10 nm ALD 4x PO_x-SiO_2 membrane, (c) uncoated Pt thin film substrate, and (d) 10 nm thick SiO_2 on 50 nm Pt thin film deposited on a p+Si (100) wafer substrate. Both ALD SiO_2 membranes were deposited at 100 °C.

To evaluate the surface morphology and confirm the structural integrity of the membranes, AFM measurements were performed. Figure 2a presents a schematic of the setup used to measure the transport properties of SiO_2, along with a representative AFM image of 10 nm thick SiO_2 and PO_x-SiO_2 membranes deposited on a 50 nm thick Pt substrate at 100 °C. The surface of the SiO_2

electrode is very smooth, having a root mean squared (rms) roughness of 1.0 nm for undoped SiO2 and 1.2 nm for PO_x-SiO_2. AFM images show that no large cracks or holes in the SiO_2 membrane in the regions analyzed. Membranes deposited at 100 °C were characterized using X-ray photoelectron spectroscopy (XPS), with the Si 2p, O 1s, and P 2p spectra shown in Figure 3. For both doped and undoped membranes, the Si 2p peak center binding energy is close to 103.5 eV, consistent with Si being present in the +4 oxidation state as SiO_2.[28]

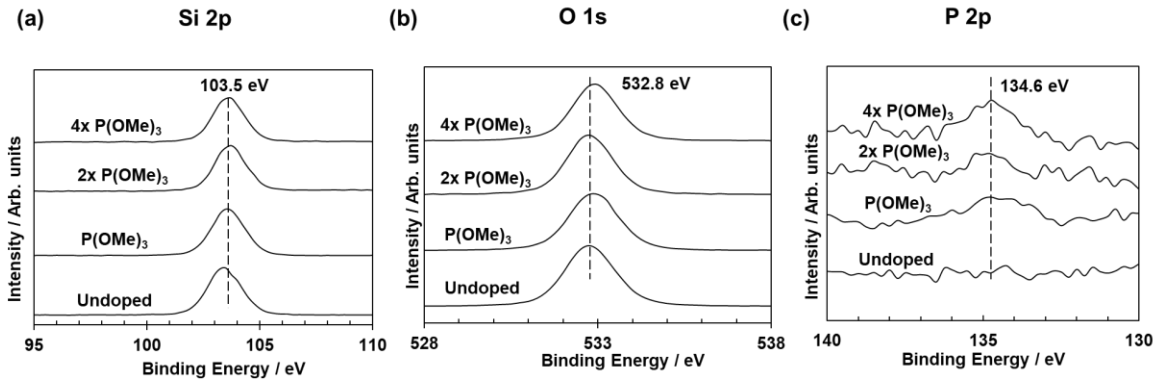

Figure 3. XPS spectra of 10nm thick undoped, 1x $P(OMe)_3$, 2x $P(OMe)_3$ and 4x $P(OMe)_3$ doped ALD SiO_2 membranes deposited on Pt/Si (100) substrate at 100°C. (a) Si 2p (b) O 1s (c) P 2p.

The areas under the peaks were used to quantify the atomic percentages of each element present in the SiO_2 matrix and atomic ratio of O:Si (Table 1). The O:Si ratio is an important parameter in determining the properties of SiO_2 membrane.[29] A O:Si ratio of 2.0 indicates a stoichiometric SiO_2 composition. However, a O:Si ratio that deviates from 2.0 can result from the presence of structural imperfections and defects like oxygen vacancies in amorphous SiO_2.[30]

Inspection of the P 2p spectra in Figure 3c reveals the presence of a distinct peak centered at ≈ 134.6 eV for the SiO_2 membranes exposed to $P(OMe)_3$ during the ALD process as described in the Methods section. A clear trend is observed with increasing $P(OMe)_3$ exposure, where the phosphorus content (P%) increases from approximately 0.3% to 0.6% in going from single (1x) to

quadruple (4x) $P(OMe)_3$ exposure, respectively. Following this convention, 1x $P(OMe)_3$ will refer to 250 ms exposure of $P(OMe)_3$, 2x $P(OMe)_3$ will refer to 500 ms exposure of $P(OMe)_3$, and 4x $P(OMe)_3$ will refer to 1000 ms exposure of $P(OMe)_3$ as the "C" component exposure time in the ABC-type ALD process.

Table 1. Atomic percent of Si, O, and P for ALD SiO_2 membrane deposited at 100 °C with different dopants and doping conditions. The atomic ratio of O:Si is also provided.

	Undoped SiO_2	1x $P(OMe)_3$	2x $P(OMe)_3$	4x $P(OMe)_3$
Oxygen	66.1	65.7	66.3	66.6
Silicon	33.9	34.0	33.3	32.9
Phosphorus	0.0	0.3	0.4	0.6
O:Si	1.9	1.9	2.0	2.0

3.2 Proton Conductivity (σ_{H^+})

Proton conductivities of Nafion and SiO_2 membranes were measured using electrochemical impedance spectroscopy (EIS) based on the difference in series resistance in the high-frequency region of the Nyquist plots between the bare Pt and the membrane-coated Pt electrodes in contact with 0.5 M H_2SO_4 at room temperature.[31] In Figure 4a, the x-intercept of the bare Pt curve represents the solution resistance (R_s), while the x-intercepts of the Nyquist curves for the membrane-coated Pt electrodes represent the combined solution resistance and membrane resistance ($R_s + R_{mem}$). By finding the difference between the x-intercepts of the bare Pt and the SiO_2 membrane curves, the total membrane H^+ resistance (R_{mem}) can be calculated. Proton conductivity (σ_{H^+}) is then determined based on R_{mem}, the membrane thickness (t_m), and membrane area (A).

$$\sigma_{H^+} = \frac{t_m}{R_{mem} \cdot A} \quad (1.)$$

The area specific membrane resistance (R_m), having units of $m\Omega \cdot cm^2$, is then calculated as the product of R_{mem} and the membrane area. R_m is a better measure of the intrinsic resistance of the membrane.

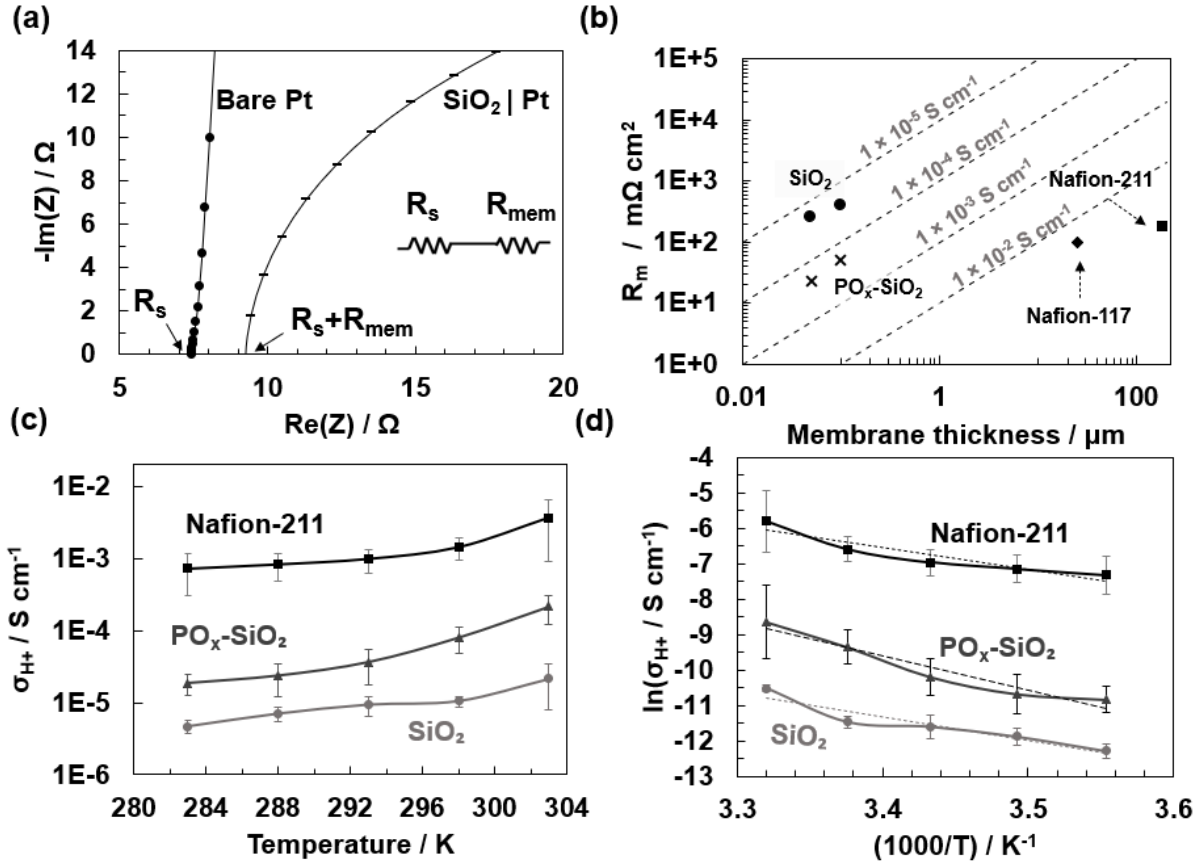

Figure 4. Measurement of membrane proton conductivities. All Nyquist plots were generated in 500 mM H_2SO_4 at room temperature and an applied potential of 0.096 V vs. RHE. (a) Nyquist plot of 50 nm ALD SiO_2 membrane-coated platinum thin film. (b) Area specific membrane resistance (R_m) as a function of membrane thickness. Dashed lines indicate constant proton conductivity values, while symbols represent resistance values calculated from experimentally determined conductivities for SiO_2, PO_x–SiO_2 deposited at 100°C, Nafion-117, and Nafion-211 membranes. (c) Proton conductivities of Nafion 211 and 50 nm PO_x-SiO_2 and 50nm SiO_2 deposited at 100 °C measured over a temperature range of 10 °C to 30 °C. Conductivities were calculated from the Nyquist plot. Error bars represent 95% confidence intervals calculated based on conductivity measurements for three different samples. (d) Representative Arrhenius plot showing the natural logarithm of proton conductivity ($\ln(\sigma_{H^+})$) versus the inverse of temperature (1000/T). The data points are fitted with a straight line across the entire temperature range.

Representative Nyquist plots measured at room temperature (≈ 22 °C) for 50 nm thick SiO_2 membranes deposited at 100 °C are shown in Figures 4a. The calculated proton conductivity of Nafion-211 is $(2.6 \pm 0.7) \times 10^{-2}$ S·cm^{-1}, while that of a 200 nm thick film of Nafion-211 ionomer is $(3.1 \pm 0.3) \times 10^{-5}$ S·cm^{-1}. The proton conductivity values for commercial Nafion-211 are consistent with those reported in the literature.[12] To further clarify the relationship between intrinsic proton conductivity and overall membrane performance, Figure 4b presents the membrane resistance as a function of membrane thickness. In this plot, the dashed lines correspond to fixed proton conductivity values, while the symbols represent resistance values calculated from the experimentally measured conductivities of the SiO_2 and PO_x–SiO_2 membranes deposited at 100 °C. As membrane resistance is an extrinsic property that scales linearly with thickness, this representation highlights that membranes with lower intrinsic conductivity can nevertheless achieve low overall resistance when fabricated at sufficiently small thicknesses.

Proton conductivities of ALD SiO_2 membranes were measured for a range of ALD temperatures and film thicknesses, with a summary of results shown in Table 2. As expected, an increase in the membrane resistance of ALD SiO_2 is observed with increasing thickness. Table 2 also presents the calculated proton conductivity values for ALD SiO_2 films of varying thicknesses deposited at 250°C, which are seen to remain relatively constant. This consistency aligns with expectations, as proton conductivity is theoretically independent of film thickness. As shown in Table 2, lower deposition temperatures lead to higher proton conductivity, which is attributed to increased incorporation of Si–OH groups within the amorphous matrix. This trend between conductivity and ALD temperature is consistent with prior observations in PECVD SiO_2 films developed for fuel cell applications. [18] Furthermore, the measured resistivities of undoped SiO2 membranes deposited at 250° C with varying thicknesses are very similar to each other, which

suggests that the transport properties of SiO_2 membranes are independent of thickness over this range of thickness. Next, the effects of PO_x incorporation into the SiO_2 matrix on proton conductivity were investigated. Figure S5 illustrates the trend in proton conductivity for SiO_2 membranes doped with varying amounts of phosphorus precursor at 175 °C. Among them, the membrane doped with 4x PO_x exhibits the highest conductivity. This trend aligns with its higher phosphorus content (0.6 at%) compared to undoped (0.0 at%), 1x PO_x (0.3 at%) doped and 2x PO_x (0.4 at%) membranes (Table 1).

Table 2. Area specific membrane resistances (R_m) and proton conductivities (σ_{H^+}) for ALD SiO_2 and PO_x-SiO_2 membranes deposited onto platinum/p^+Si (100) substrates. Error bars represent 95% confidence intervals based on three independent samples of the same sample type. All measurements were carried out in 0.5 M H_2SO_4 and at room temperature.

Membrane Thickness (nm)	**Dopant**	**Deposition Temperature (°C)**	**R_m ($m\Omega \cdot cm^2$)**	**Proton Conductivity ($S \cdot cm^{-1}$)**
10	None	250	53±20	$(2.1\pm0.8) \times 10^{-5}$
50	None	250	313±52	$(1.6\pm0.3) \times 10^{-5}$
250	None	250	1522±230	$(1.7\pm0.2) \times 10^{-5}$
10	None	100	17±10	$(8.4\pm1.9) \times 10^{-5}$
50	4x PO_x	100	23±11	$(2.2\pm0.7) \times 10^{-4}$
10	4x PO_x	175	57±26	$(2.0\pm0.9) \times 10^{-5}$
10	2x PO_x	175	250±44	$(4.1\pm0.8) \times 10^{-6}$
10	1x PO_x	175	382±57	$(2.3\pm0.9) \times 10^{-6}$
10	None	175	354±57	$(2.8\pm0.2) \times 10^{-6}$

The temperature dependence of proton conductivity over the range 10 °C to 30 °C was also measured for a sub-set of samples using a constant temperature bath. Results for Nafion-211, 50 nm PO_x-SiO_2, and undoped 50 nm SiO_2 (both deposited at 100 °C) are shown in Figure 4c. The

natural logarithm of σ_{H^+} was plotted as a function of the inverse temperature (1000/T) to create an Arrhenius plot (Figure 4d) and the slope of this plot was used to determine the activation energy (E_a) for proton conduction. The linear relationship between ln (σ_{H^+}) and 1/T suggests that σ_{H^+} follows the Arrhenius equation:

$$\sigma = \sigma_0 \exp\left(-\frac{E_a}{kT}\right) \quad (2.)$$

where σ_0 is the pre-exponential factor, E_a is the activation energy, k is the Boltzmann constant, and T is the temperature in Kelvin. Within the temperature range of 10 °C to 30 °C, the activation energy was determined to be 0.42±0.07 eV (40.8±6.7 kJ mol^{-1}) for Nafion-211, 0.58±0.04 eV (56.1±3.9 kJ mol^{-1}) for 50 nm SiO_2, and 0.50±0.09 eV (48.6±8.7 kJ mol^{-1}) for 50 nm PO_x-SiO_2. E_a for Nafion-211 falls within the typical range reported for hydrated Nafion membranes (0.1–0.5 eV), suggesting that H^+ transport is primarily taking place through a Grotthuss-like mechanism facilitated by proton hopping between sulfonate groups and water molecules, with the exact energy influenced by hydration levels.[32-35] In contrast, the 0.58 eV activation energy for SiO_2 is higher than the expected range for Grotthuss-dominated transport in hydroxylated materials (0.1–0.4 eV)[36], implying that proton conduction likely involves a mixed mechanism, where vehicular diffusion of hydronium ions contributes significantly alongside limited Grotthuss-type hopping between adsorbed water and surface –OH groups.[37] The intermediate value for PO_x-SiO_2 (0.50 eV) suggests that phosphonate functionalization enhances proton mobility compared to pure SiO_2, possibly by introducing additional proton-hopping sites,[23] though the activation energy remains higher than that of well-hydrated Nafion. This interpretation is well aligned with prior studies on phosphate-containing and silica-based amorphous systems. Nogami *et al.*[38] described proton conduction in phosphate glass networks using a mixed framework, where proton hopping

along hydrogen-bonded P–OH sites coexists with water-assisted vehicular transport, even in dense matrices. Bhusari *et al.*[39] reported that phosphorus incorporation into SiO_2 enhances proton conductivity through the introduction of phosphate-related proton-conducting sites, consistent with hopping-based transport supplemented by hydration effects. Related studies by Namazi and Ahmadi[40] and by Yin *et al.*[41] further showed that chemically modified silica-based networks can sustain efficient proton transport under hydrated conditions through hydrogen-bonded networks, which provide the structural framework supporting both proton hopping and water-assisted vehicular diffusion. While the proton conductivity of $P(OMe)_3$-SiO_2 could only be measured below 30°C due to its tendency to delaminate from the Pt thin film substrate at elevated temperatures, the comparative data for Nafion-211 and SiO_2 collected between 30-60°C (Figure S6) show consistent trends with the low-temperature measurements. Although the intrinsic proton conductivity of silicon oxide–based membranes remains lower than that of perfluorosulfonic acid ionomers, several strategies may be employed to further enhance proton transport. One approach is increasing the phosphorus dopant concentration within the oxide network, thereby increasing the density of phosphate-related proton-conducting sites. Proton conductivity may also be improved by optimizing hydration and water retention within the membrane, as increased bound water content is known to facilitate proton transport through a combination of hopping and vehicular mechanisms.[42] In addition to compositional and hydration-based strategies, increasing operating temperature represents another effective means of enhancing proton conductivity in PO_x–SiO_2 membranes. As shown in Figure 4c, proton conductivity increases with temperature for both SiO_2 and PO_x–SiO_2, consistent with thermally activated transport behavior. Importantly, oxide-based membranes are expected to exhibit substantially greater thermal stability than polymer electrolytes such as Nafion, whose conductivity and mechanical integrity degrade at temperatures approaching

or exceeding ≈80 °C due to dehydration and polymer softening.[43] In contrast, amorphous oxide membranes are not subject to polymer relaxation or melt-like transitions and are therefore expected to maintain structural integrity at significantly higher temperatures,[44] suggesting the potential for stable operation in the 80–150 °C range where proton conductivity is further enhanced.

3.3 Hydrogen Permeability (P_{H_2})

The hydrogen permeabilities (P_{H_2}) of SiO_2 membranes were determined using a rotating disc electrode (RDE) setup, which allowed for the measurement of mass-transport limited current densities associated with the hydrogen oxidation reaction (HOR) occurring at the buried interface between the SiO_2 membrane and the thin-film Pt substrate. H_2 must first diffuse across a diffusion boundary layer (DBL) and then through the membrane before the reaction can occur. To deconvolute the mass transfer resistance associated with the DBL from that associated with the membrane, the mass transfer limiting HOR current density (i_{lim}) is determined from a linear sweep voltammetry (LSV) curve measured for a bare Pt electrode ($i_{lim,Pt}$).

This limiting current is inversely related to the mass transfer resistance of the DBL. Next, the limiting HOR current density of a membrane coated electrode ($i_{lim,SiO_2|Pt}$) is recorded. As seen in Figure 5b, the HOR limiting current observed in LSV curves drops significantly for SiO_2-coated Pt thin films, which is attributed to the additional mass transfer resistance introduced by the presence of the membrane. The flat, potential-independent nature of these LSV curves is consistent

with the reaction rate being limited solely by diffusion of the reactant, H_2, to the buried interface, rather than reaction kinetics and/or migration of H^+.

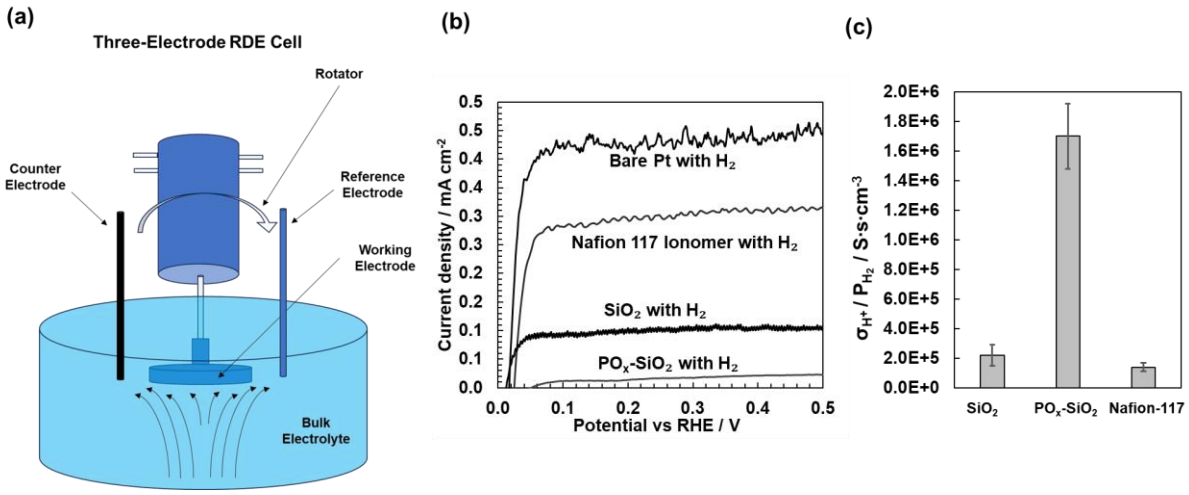

Figure 5. (a) Schematic illustration of the experimental configuration used to evaluate hydrogen permeability through SiO_2-based membranes, depicting a SiO_2 membrane–coated Pt/Si wafer operated in a rotating disk electrode (RDE) setup. (b) Linear sweep voltammetry (LSV) curves of ALD 10 nm SiO_2 and 10 nm 4x PO_x-SiO_2 membrane-coated platinum/silicon (Si) wafer at a rotation speed of 600 rpm in H2-saturated 0.5 M H_2SO_4. (c) Ratio of proton conductivity to hydrogen permeability for PO_x-SiO_2 and SiO_2 deposited at 100°C and Nafion based membranes.

Since the mass transfer resistances for H_2 transport across the membrane and DBL are in series, the limiting currents associated with each are related as follows:[45]

$$\frac{1}{i_{lim,SiO_2|Pt}} = \frac{1}{i_{lim,Pt}} + \frac{1}{i_{lim,SiO_2}} \qquad (3.)$$

where i_{lim,SiO_2} is the limiting current density solely associated with the SiO_2 membrane.

i_{lim,SiO_2} may be calculated from Equation (3.) based on the measured values of $i_{lim,Pt}$ and $i_{lim,SiO_2|Pt}$ for the bare Pt and SiO_2|Pt electrodes, respectfully. Next, P_{H_2} is calculated using

Equation (4.), which is based on Faraday's law and Fick's first law for steady state operation of the membrane-coated electrode, assuming a vanishing H_2 concentration at the Pt surface:[46]

$$i_{lim,SiO_2} = -nFP_{H_2}\frac{C_{H_2,b}}{t_m} \quad (4.)$$

where n is the number of electrons, F is the Faraday constant (96485 C mol^{-1}), $C_{H_2,b}$ is the concentration of species H_2 in the electrolyte, and t_m is the thickness of the membrane. A limitation of measuring HOR current density arises when the film is too thick, resulting in a low signal. To address this, Nafion-117 ionomer with a reduced thickness of 208 nm was prepared to enable accurate HOR measurement. Based on the procedure outlined above, P_{H_2} values were determined for 10 nm SiO_2 deposited at 100 °C ((3.8±0.4) $\times 10^{-10}$ $cm^2 \cdot s^{-1}$), 10 nm 4x PO_x-SiO_2 deposited at 100 °C ((1.3±0.1) $\times 10^{-10}$ $cm^2 \cdot s^{-1}$), and 208 nm Nafion117 ((2.0± 0.8) $\times 10^{-7}$ $cm^2 \cdot s^{-1}$). These figures are consistent with our previous reports in literature.[46, 47] The substantially lower hydrogen permeability of SiO_2-based membranes compared to Nafion arises from intrinsic structural differences between the two materials. Amorphous SiO_2 forms a dense, highly cross-linked inorganic network that restricts molecular hydrogen transport, whereas Nafion contains larger nanoscopic hydrated ionic channels that facilitate gas diffusion. The ALD-deposited SiO_2 films exhibit extremely low porosity, comparable to that of dense thermal oxides,[48] whereas hydrated Nafion has an estimated porosity of roughly 28%. [19] This difference in porosity reflects the smaller free volume in SiO_2, which limits hydrogen transport through the membrane via the solution–diffusion mechanism. Consequently, the lower hydrogen permeability of SiO_2-based membranes compared to Nafion membrane enables the use of thinner layers while maintaining low hydrogen crossover. This thickness advantage directly reduces membrane resistance, a critical factor in water electrolysis where ohmic losses must be minimized. To provide a more integrated

assessment of membrane performance, Figure 5c presents the ratio of proton conductivity to hydrogen permeability. Unlike proton conductivity alone, σ_{H^+}/P_{H_2} captures the simultaneous requirements of efficient proton transport and effective hydrogen crossover suppression that ultimately govern allowable membrane thickness and overall membrane resistance in electrolyzer operation. As shown in Figure 5c, PO_x–SiO_2 membranes exhibit higher σ_{H^+}/P_{H_2} values than Nafion, reflecting their ability to maintain adequate proton conduction while dramatically reducing hydrogen permeability.

3.4 Electrical Resistivity (ρ_{e^-})

Electrical resistivities (ρ_{e^-}) of SiO_2 membranes were determined from current-voltage (I-V) and EIS measurements carried out in the absence of electrolyte using the test platform illustrated in the Figure 6a. These samples were identical to those used for the proton conductivity and hydrogen permeability measurements except that an electrical top contact in the form of an additional Pt layer was deposited directly onto the as-deposited SiO_2 membrane. The total electrical resistance (R_{e^-}) of each sample was determined from the slope of the dry I-V curve, according to Ohm's law:

$$R_{e^-} = \frac{dV}{dI} \tag{5.}$$

The electrical resistivity (ρ_{e^-}) was then calculated from R_{e^-}, the area of the membrane (A), and the thickness of the membrane (t_m):

$$\rho_{e^-} = \frac{R_{e^-} \cdot A}{t_m} \tag{6.}$$

Electrical conductivity measurements were also confirmed by EIS. In this setup, a leaky capacitor model is fit to the EIS data to determine ρ_{e^-}. The equivalent circuit for the leaky

capacitor model is shown in Figure 6b. In this circuit, R1 represents the contact resistance and C is the capacitance of the dry membrane, which is in parallel with a second resistance, R2, that represents an ohmic resistance associated with electrons "leaking" through the dielectric SiO_2 layer. The resistance can be obtained by fitting the Nyquist Plot shown in Figure 6b. EIS and I-V curve measurements give ρ_{e^-} results that are in good agreement with each other. The apparent variation in measured resistance across different membrane thicknesses is expected, since electrical resistance is an extrinsic property that scales linearly with membrane thickness, as described by Equation (6).

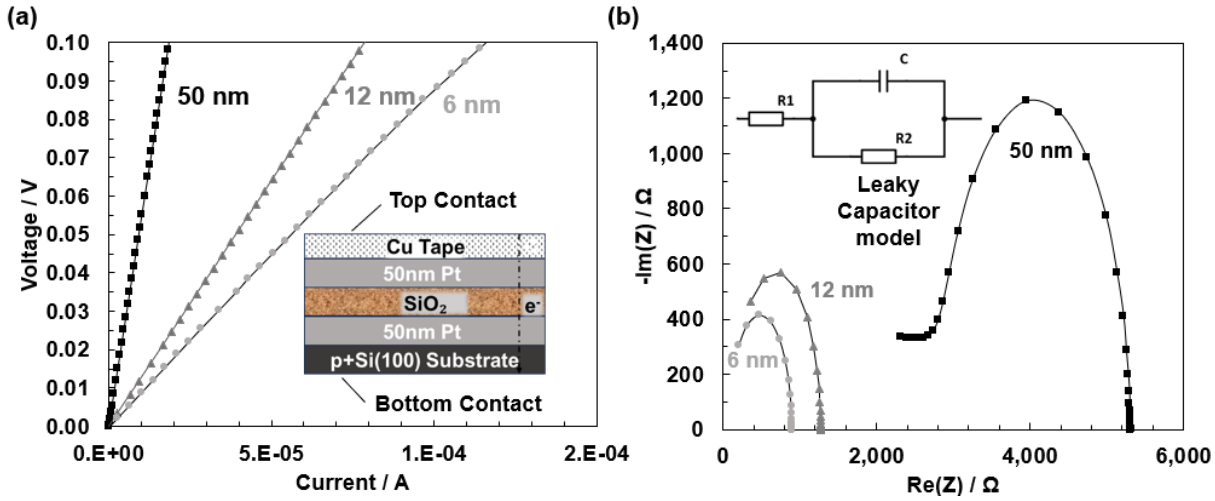

Figure 6. (a) I-V curve for electrolysis cell based on 6 nm, 12 nm, 50 nm ALD SiO_2 membrane deposited at 100 °C and Pt thin film electrodes in the absence of electrolyte and at room temperature. (b) Equivalent circuit of leaky capacitor model used to measure electrical resistivity and Nyquist plot for the same sample with dry EIS measurement.

For a given intrinsic conductivity, thicker SiO_2 membranes inherently exhibit higher resistance. Figure 6a clearly shows this expected trend—resistance increases proportionally with film thickness—confirming the reproducibility and consistency of our measurements. The conductivity values, derived from the slope of R vs. t_m, remain constant across all samples — $(1.2 \pm 0.4) \times 10^8$ Ω·cm for 6 nm SiO_2, $(9.1 \pm 0.6) \times 10^7$ Ω·cm for 12 nm SiO_2, and $(1.1 \pm 0.3) \times 10^8$ Ω·cm for 250 nm SiO_2— indicating that the observed variations reflect geometric scaling rather

than experimental variability. The calculated average ρ_{e^-} for SiO_2 across all thickness is (1.1±0.7) $\times 10^8$ Ω·cm, which is in agreement with literature.[49, 50] The incorporation of PO_x has a minimal effect on electrical resistivity, as shown by the value reported for PO_x-SiO_2 in Table 3.

3.5 Comparing Key Performance Metrics of SiO_2 and Nafion Membranes

It is necessary to analyze all membrane transport properties in relation to the key performance metrics of an electrolyzer that impact efficiency and safety. Here, the influence of membrane transport properties on H_2 crossover rates, electrical leakage currents, and the ratio of σ_{H^+}/P_{H_2} are considered. σ_{H^+}/P_{H_2} is a useful figure of merit that can be used to predict the minimum required membrane thickness for safe operation while maximizing electrolyzer efficiency.[9]

When designing thin membranes for PEM electrolyzers, a crucial safety issue to consider is the crossover of H_2 from the cathode to the anode, particularly at large pressure differentials (Δp_{H_2}) between the electrodes. The lower limit of H_2 crossover (as a percentage of H_2 generated) is closely linked to H_2 permeability (P_{H_2}), making it essential to translate the measured P_{H_2} into crossover values. This evaluation is necessary to assess the performance of thin SiO_2 membranes in practical electrolyzers. In the absence of defects, the steady state flux of H_2 across a planar membrane (J_{H_2}) can be approximated by Fick's law,[8] which is shown in Equation 7:

$$J_{H_2} = \frac{P_{H_2} \cdot \Delta C_{H_2}}{t_m} = \frac{P_{H_2} \cdot \Delta p_{H_2}}{t_m \cdot R_g \cdot T} \tag{7.}$$

where ΔC_{H_2} is the concentration difference across the membrane, Δp_{H_2} is the partial pressure difference across the membrane, R_g is the gas constant, and T is the temperature. The hydrogen crossover rate expressed as a percentage of the total rate of H_2 production (%CR) is calculated

using Equation 8, which compares J_{H_2} to the rate of H_2 production described by Faraday's law of electrolysis. The equation also accounts for membrane thickness, hydrogen partial pressure difference, temperature, and permeability. Assuming a H_2 partial pressure difference of Δp_{H_2} =14.8 bar and an operating current density of i = 1.5 A·cm^{-2}, the calculated crossover rate (0.15%) of the best-performing sample in Table 3, 50 nm 4x PO_x-SiO_2 deposited at 100 °C, is below 1%. This satisfies ISO 22734 safety requirements for electrolysis systems, where the H_2 content in the anode stream must not exceed 50% of the lower flammability limit (LFL) for hydrogen-oxygen mixtures.[51]

$$\%CR = J_{H_2} / \left(\frac{i}{2F}\right) = \frac{P_{H_2} \cdot \Delta p_{H_2} \cdot 2F}{i \cdot t_m \cdot R_g \cdot T} \tag{8.}$$

Another important factor to consider is electrical leakage current across the membrane. If the leakage current density approaches or exceeds a few percent of the total current density (both ionic and electrical), it will detrimentally affect electrolyzer efficiency.[9] This inefficiency occurs because the "crossed over electrons" are dissipated as heat. The amount of electron crossover highly depends on the membrane's electrical conductivity (σ_{e^-}) as shown in Equation 9:

$$\%i_{e,leakage} = \left(\frac{V_m}{R_{m,e}}\right) / i = \frac{V_m \cdot \sigma_{e^-}}{i \cdot t_m} \tag{9.}$$

Assuming an operating voltage of 2 V and an operating current density of 1.5 A·cm^{-2}, $\%i_{e,leakage}$ is calculated to be 0.07% and 0.02 % for 50 nm thick undoped SiO_2 and 50 nm thick PO_x-SiO_2 membranes deposited at 100 °C, respectively. This analysis shows that the electrical resistivities of dielectric ALD SiO_2 membranes are more than sufficient to prevent significant parasitic electrical leakage currents, even at nanoscopic thicknesses that are orders of magnitude lower than

Nafion. In contrast, a Nafion-117 membrane is predicted to give a value of $\%i_{e,leakage}$ = 6.5 %, which is unacceptably high.

Table 3 outlines the key performance metrics of the SiO_2 membranes , comparing with performance across critical properties compared to Nafion membranes. The 50 nm PO_x-SiO_2 membrane is seen to outperform Nafion-117 in terms of membrane resistance, hydrogen permeability, and electrical resistivity. Importantly, the ratio σ_{H^+}/P_{H_2} for this PO_x-SiO_2 membrane is 10 times greater than that for Nafion-117, indicating that higher water electrolysis efficiency can be obtained using PO_x-SiO_2-based PEM electrolyzers compared to Nafion-based PEM electrolyzers while maintaining safe operating conditions.[9]

Table 3. Comparison of critical properties of SiO_2 and PO_x-SiO_2 membranes deposited at 100 °C to hydrated Nafion-117 measured at T = 22 ºC. Error bars represent 95% confidence interval based on repeat measurements of three different samples for each sample type.

Membrane	**R_m ($m\Omega \cdot cm^2$)**	**σ_{H^+} ($S \cdot cm^{-1}$)**	**%CR**	**P_{H_2} ($cm^2 \cdot s^{-1}$)**	**ρ_{e^-} ($\Omega \cdot cm$)**	**$\%i_{e,leakage}$**	**σ_{H^+}/P_{H_2} ($S \cdot s \cdot cm^{-3}$)**
10 nm SiO_2	17.2±9.7	$(8.4\pm1.9)\times10^{-5}$	2.9%	$(3.8\pm0.4)\times10^{-10}$	$(8.6\pm0.7)\times10^{8}$	0.12%	2.2×10^{5}
50 nm PO_x-SiO_2	23.4±11.2	$(2.2\pm0.7)\times10^{-4}$	0.15%	$(1.3\pm0.1)\times10^{-10}$	$(5.8\pm1.2)\times10^{8}$	0.02 %	1.7×10^{6}
Nafion-117	180	2.7×10^{-2}	0.09%	$(2.0\pm0.7)\times10^{-7}$	$(9.1\pm0.8)\times10^{5}$	6.5%	1.4×10^{5}

3.6 Chip Scale PEM Water Electrolyzer with Nanoscale SiO_2 Membrane

A miniaturized “chip scale” electrolyzer test platform with a 0.1 cm² active area was used to demonstrate the viability of using nanoscale SiO_2 membranes for efficient water electrolysis using a “zero-gap” membrane electrode assembly (MEA) design wherein the membrane is sandwiched between the electrodes. The design integrates several critical components that mimic the

operational conditions of a full-scale PEM electrolyzer while enabling precise experimental control of interfacial area and comparison of performance for different membrane types.

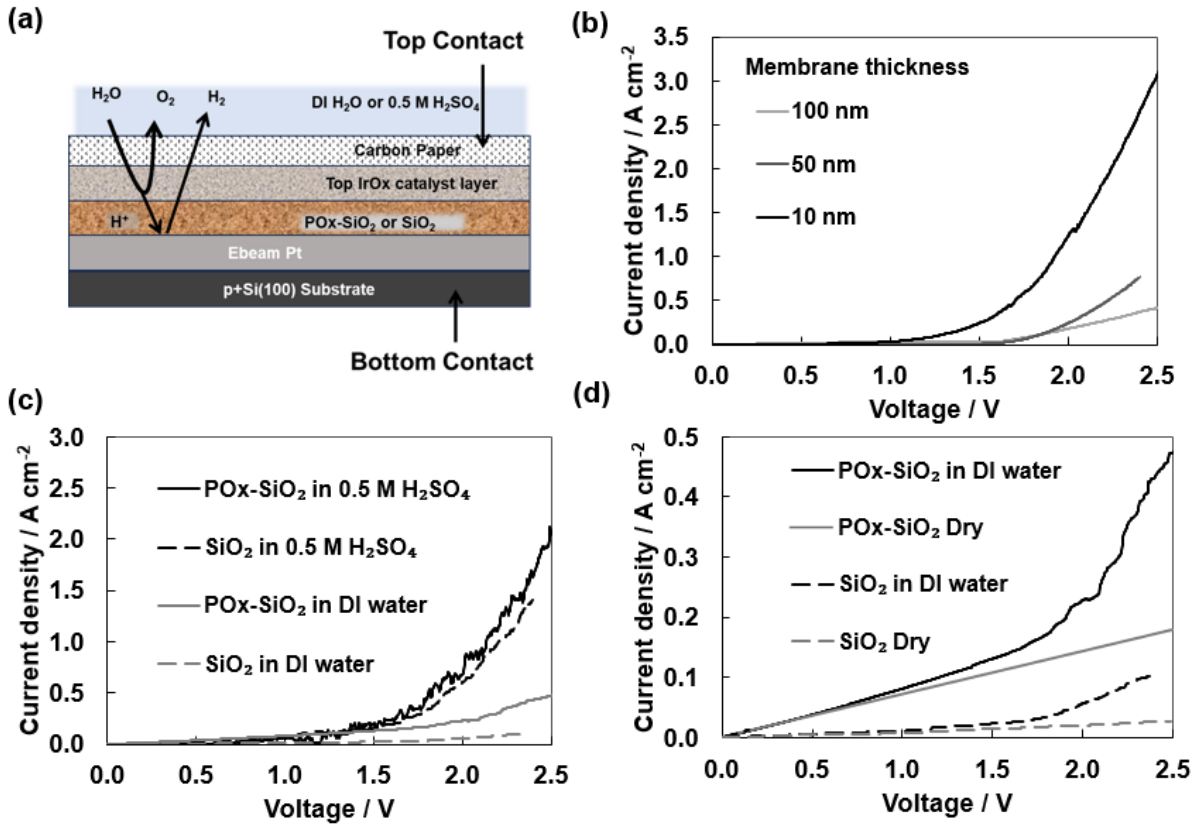

Figure 7. (a) Schematic side-view of a chip-scale electrolyzer test platform. (b) I-V curves measured in 0.5 M H_2SO_4 for zero-gap electrolyzers based on undoped ALD SiO_2 membranes with varying thicknesses (10 nm, 50 nm, and 100 nm) deposited at 250 °C. (c) I-V curves measured in 0.5 M H_2SO_4 and DI water for zero-gap electrolyzers based on 100 nm thick ALD POx-SiO_2 and 100 nm ALD SiO_2 membranes deposited at 100 °C. (d) Comparison of the I-V curves measured in DI water from (c) to I-V curves for the same samples measured in the absence of electrolyte "Dry" to determine electrical leakage current.. Current densities are normalized to the geometric area of the MEA exposed to the electrolyte. All measurements were carried out at room temperature using a scan rate of 10 $mV \cdot s^{-1}$ and electrolyte flow rate of 20 $mL \cdot min^{-1}$.

Figure 7a provides a detailed schematic of the platform's architecture, showing its key elements from top to bottom: a carbon paper-based gas diffusion layer, an IrO_x-based anode catalyst layer (0.2 $mg_{Ir}\,cm^{-2}$) where the oxygen evolution reaction (OER) occurs, a thin (10 nm - 100 nm thick) ALD SiO_2 membrane, a smooth 50 nm thick Pt thin film that serves as the cathode

catalyst for the hydrogen evolution reaction (HER), and a degenerately-doped Si(100) wafer (i.e. "chip") substrate. Electrolyzer chips containing different SiO_2 membranes were then integrated into a custom flow-cell (Figure S9) that allowed for removal of gaseous products by flowing either DI water or 0.5 M H_2SO_4 through the cell. Although this small-scale chip-based electrolyzer doesn't allow for separate collection of O_2 and H_2, making it impractical for most real-world applications, it does serve as a useful test platform for proof-of-principle electrolysis experiments with well-defined interfaces without having to deal with the complexities of depositing the oxide membrane on a porous substrate.

To assess the performance of the chip-scale electrolyzer, current density-voltage (I-V) measurements (i.e. polarization curves) were measured at room temperature in either DI water or 0.5 M H_2SO_4, with the results presented in Figures 7b-7d. In Figure 7b, it is seen that the current density recorded for electrolyzers based on undoped SiO_2 membranes increases monotonically as the membrane thickness decreases, demonstrating a clear inverse correlation between membrane thickness and membrane resistance. Remarkably, the electrolyzer based on a 10 nm thick undoped SiO_2 membrane—over 4 orders of magnitude thinner than Nafion-117—is still capable of producing I-V curves that are characteristic of water splitting without exhibiting exorbitant electronic leakage current. This result can be attributed to (i) the uniform, defect-free nature of the dense ALD SiO_2 membranes deposited on the planar chip-based substrate (Figure 2a) and (ii) their high electronic resistivity (Table 3).

Figure 7c compares I-V behavior of 100 nm thick ALD PO_x–SiO_2 and undoped SiO_2 membranes (all deposited by ALD at 100 ºC) in both 0.5 M H_2SO_4 and DI water. For both membrane types, higher current densities are achieved in 0.5 M H_2SO_4 compared to DI water, indicating that the presence of mobile counterions (HSO_4^-) in the 0.5 M H_2SO_4 electrolyte enhances

the ionic conductivity of the SiO_2 membranes. For undoped SiO_2, this result is not surprising, as the absence of negatively charged ion exchange centers necessitates the addition of anions from a supporting electrolyte to support charge neutralization of H^+ within the membrane. For the PO_x-doped membranes, the fact that the polarization curve measured in DI water is significantly worse than that measured in 0.5 M H_2SO_4 indicates that the ion exchange capacity of the PO_x dopants is relatively low. This finding motivates the need for further development of doped oxide membranes with higher dopant concentrations and/or different dopants.

Nonetheless, the electrolyzers based on PO_x-SiO_2 membranes outperform undoped SiO_2 in both 0.5 M H_2SO_4 and DI water. This enhanced performance is consistent with the results that the PO_x-SiO_2 membranes exhibit higher proton conductivity than undoped membranes (Table 2). Figure 7d shows the dry I-V curves overlaid with the I-V curves measured in DI water, demonstrating that electrolyzers based on both types of membranes clearly exhibit water splitting current above the baseline electrical leakage current. It is important to note that the current attributed to water electrolysis, given by the difference in current measured in DI water compared to the dry state, is 2.5 times larger for the electrolyzer based on the PO_x-SiO_2 membrane compared to the undoped SiO_2 membrane. Although the I-V curves in DI water for this electrolyzer are significantly worse than those for conventional Nafion-based PEM electrolyzers operating in DI water, the results of Figure 7d indicate that the PO-dopants within the SiO_2 membranes are able to provide some ion exchange capacity for H^+ transfer during water electrolysis in the absence of a supporting electrolyte.

Table 4. Comparison of proton conductivity values obtained from EIS measurements of membrane-coated electrodes and I-V curves for chip-scale electrolyzers recorded at room temperature in 0.5 M H_2SO_4. Error bars indicate a 95% confidence interval based on modeling.

Sample	**Deposition Temperature**	**σ_{H^+} (S cm^{-1}) Membrane-coated electrodes**	**σ_{H^+} (S cm^{-1}) Chip scale Electrolyzer**
100 nm SiO_2	250 °C	$(1.7\pm0.2) \times10^{-5}$	$(1.1\pm0.4) \times10^{-5}$
100 nm SiO_2	100 °C	$(8.4\pm1.9) \times10^{-5}$	$(3.6\pm0.4) \times10^{-5}$
100nm PO_x-SiO_2	100 °C	$(2.2\pm0.7) \times10^{-4}$	$(2.3\pm0.2) \times10^{-4}$

To check for consistency between the H^+ conductivity measurements for the model membrane-coated electrodes and the chip-scale electrolyzers, the I-V curves in Figure 7b-d were fitted using a simple 0-dimensional model (See Supporting Information section 4) to extract proton conductivities for each membrane (Table 4). For all samples analyzed, close agreement is seen between conductivity values calculated from EIS half-cell measurements using the membrane-coated electrodes (Figure 4) and from two electrode I-V curves recorded for the chip-scale electrolyzer. The strong agreement in H^+ conductivities indicates that the SiO_2 membranes exhibit similar H^+ transport behavior in the two different set-ups. Although the best polarization curve shown in Figure 7c for the SiO_2 -based POM electrolyzers does not match the performance of a conventional PEM electrolyzer,[8] it is important to note that this result was obtained with significantly lower specific areas for the anode and cathode catalysts and used unoptimized porous transport layers. With further development of sub-micron thick SiO_2 membranes and their application to porous electrode supports rather than Si wafer substrates, POM electrolyzers offer a promising option for high efficiency, low-temperature water electrolysis using PFAS-free membranes that can replace Nafion.

IV. Conclusions

This study has demonstrated that sub-micron thick proton-conducting SiO_2 membranes deposited by ALD at low temperatures (100 ºC – 250 ºC) possess a combination of key transport properties that make them attractive alternatives to PFAS-based polymeric ion exchange membranes like Nafion. Most notably, this work shows that ALD SiO_2 membranes doped with phosphorous can achieve a ratio of H^+ conductivity to H_2 permeability that is 10 – 20 times greater than Nafion, meaning that water electrolyzers based on thickness-optimized SiO_2 membranes should be capable exceeding the performance of Nafion-based PEM electrolyzers while maintaining safe operating conditions. Additionally, all the SiO_2 membranes tested exhibit low electrical resistance, allowing them to limit electrical leakage current to acceptable levels despite their nanoscale thickness. Moreover, chip-scale electrolyzer tests confirm the trends in transport properties measured for undoped and phosphorous-doped SiO_2 membranes while showing that the presence of PO_x dopants—introduced during the ALD process—can serve as ion exchange centers that enable water electrolysis from DI water in the absence of a supporting electrolyte. The performance of these proton conducting oxide membrane (POM) devices still lags conventional Nafion-based PEM electrolyzers, especially when using DI water. Nevertheless, measurements carried out with the chip-scale electrolyzer platform demonstrate that high current density (> 1 A cm^{-2}) water electrolysis can be achieved at low temperature using PFAS-free, sub-micron thick POMs. These findings suggest that SiO_2 membrane-based electrolyzers offer a promising and efficient alternative to conventional PEM electrolyzers.

V. Acknowledgements

The information, data, or work presented herein was funded by the Advanced Research Projects Agency-Energy (ARPA-E), U.S. Department of Energy, under Award Number DE-AR0001567.

The views and opinions of authors expressed herein do not necessarily state or reflect those of the United States Government or any agency thereof. Use of the Rame-Hart Model 260 goniometer provided by Yip Lab at Columbia University

V. Reference

(1) Ahmed, A.; Al-Amin, A. Q.; Ambrose, A. F.; Saidur, R. Hydrogen fuel and transport system: A sustainable and environmental future. *International Journal of Hydrogen Energy* **2016**, *41* (3), 1369–1380. DOI: 10.1016/j.ijhydene.2015.11.084.
(2) Bhandari, R.; Adhikari, N. A comprehensive review on the role of hydrogen in renewable energy systems. *International Journal of Hydrogen Energy* **2024**, *82*, 923–951. DOI: 10.1016/j.ijhydene.2024.08.004.
(3) Carmo, M.; Fritz, D. L.; Mergel, J.; Stolten, D. A comprehensive review on PEM water electrolysis. *International Journal of Hydrogen Energy* **2013**, *38* (12), 4901–4934. DOI: 10.1016/j.ijhydene.2013.01.151.
(4) Phillips, R.; Edwards, A.; Rome, B.; Jones, D. R.; Dunnill, C. W. Minimising the ohmic resistance of an alkaline electrolysis cell through effective cell design. *International Journal of Hydrogen Energy* **2017**, *42* (38), 23986–23994. DOI: 10.1016/j.ijhydene.2017.07.184.
(5) Muhsen, H.; Alshawabkeh, M.; Al-Mahmodi, M.; Ghanem, A.; Al-Halhouli, A. A. Sensitivity analysis of electrodes spacing media for evaluating alkaline electrolyzer performance through CFD modeling. *Renewable Energy Focus* **2024**, *49*, 100575. DOI: 10.1016/j.ref.2024.100575.
(6) Pashchenko, D. Green hydrogen as a power plant fuel: What is energy efficiency from production to utilization? *Renewable Energy* **2024**, *223*, 120033. DOI: 10.1016/j.renene.2024.120033.
(7) Gaines, L. G. T. Historical and current usage of per- and polyfluoroalkyl substances (PFAS): A literature review. *American Journal of Industrial Medicine* **2023**, *66* (5), 353–378. DOI: 10.1002/ajim.23362.
(8) Bernt, M.; Schröter, J.; Möckl, M.; Gasteiger, H. A. Analysis of Gas Permeation Phenomena in a PEM Water Electrolyzer Operated at High Pressure and High Current Density. *Journal of The Electrochemical Society* **2020**, *167* (12), 124502. DOI: 10.1149/1945-7111/abaa68.
(9) Cohen, L. A.; Weimer, M. S.; Yim, K.; Jin, J.; Fraga Alvarez, D. V.; Dameron, A. A.; Capuano, C. B.; Ouimet, R. J.; Fortiner, S.; Esposito, D. V. How Low Can You Go? Nanoscale Membranes for Efficient Water Electrolysis. *ACS Energy Letters* **2024**, *9* (4), 1624–1632. DOI: 10.1021/acsenergylett.4c00170.
(10) Luo, X.; Lau, G.; Tesfaye, M.; Arthurs, C. R.; Cordova, I.; Wang, C.; Yandrasits, M.; Kusoglu, A. Thickness Dependence of Proton-Exchange-Membrane Properties. *Journal of The Electrochemical Society* **2021**, *168* (10), 104517. DOI: 10.1149/1945-7111/ac2973.
(11) Tsampas, M. N.; Pikos, A.; Brosda, S.; Katsaounis, A.; Vayenas, C. G. The effect of membrane thickness on the conductivity of Nafion. *Electrochimica Acta* **2006**, *51* (13), 2743–2755. DOI: 10.1016/j.electacta.2005.08.021.
(12) Peron, J.; Mani, A.; Zhao, X.; Edwards, D.; Adachi, M.; Soboleva, T.; Shi, Z.; Xie, Z.; Navessin, T.; Holdcroft, S. Properties of Nafion® NR-211 membranes for PEMFCs. *Journal of Membrane Science* **2010**, *356* (1-2), 44–51. DOI: 10.1016/j.memsci.2010.03.025.

(13) Kreitmeier, S.; Michiardi, M.; Wokaun, A.; Büchi, F. N. Factors determining the gas crossover through pinholes in polymer electrolyte fuel cell membranes. *Electrochimica Acta* **2012**, *80*, 240–247. DOI: 10.1016/j.electacta.2012.07.013.
(14) Daryaei, A.; Miller, G. C.; Willey, J.; Roy Choudhury, S.; Vondrasek, B.; Kazerooni, D.; Burtner, M. R.; Mittelsteadt, C.; Lesko, J. J.; Riffle, J. S.; et al. Synthesis and Membrane Properties of Sulfonated Poly(arylene ether sulfone) Statistical Copolymers for Electrolysis of Water: Influence of Meta- and Para-Substituted Comonomers. *ACS Applied Materials & Interfaces* **2017**, *9* (23), 20067–20075. DOI: 10.1021/acsami.7b02401.
(15) Ghassemzadeh, L.; Pace, G.; Di Noto, V.; Müller, K. Effect of SiO_2 on the dynamics of proton conducting [Nafion/(SiO_2)X] composite membranes: a solid-state 19F NMR study. *Physical Chemistry Chemical Physics* **2011**, *13* (20), 9327. DOI: 10.1039/c0cp02316g.
(16) Rodgers, M. P.; Shi, Z.; Holdcroft, S. Transport properties of composite membranes containing silicon dioxide and Nafion®. *Journal of Membrane Science* **2008**, *325* (1), 346–356. DOI: 10.1016/j.memsci.2008.07.045.
(17) Meng, Y.; Gao, J.; Zhao, Z.; Amoroso, J.; Tong, J.; Brinkman, K. S. Review: recent progress in low-temperature proton-conducting ceramics. *Journal of Materials Science* **2019**, *54* (13), 9291–9312. DOI: 10.1007/s10853-019-03559-9.
(18) Moore, C. W.; Li, J.; Kohl, P. A. Microfabricated Fuel Cells with Thin-Film Silicon Dioxide Proton Exchange Membranes. *Journal of The Electrochemical Society* **2005**, *152* (8), A1606. DOI: 10.1149/1.1949027.
(19) Rao, A. S.; Rashmi, K. R.; Manjunatha, D. V.; Jayarama, A.; Prabhu, S.; Pinto, R. Pore size tuning of Nafion membranes by UV irradiation for enhanced proton conductivity for fuel cell applications. *International Journal of Hydrogen Energy* **2019**, *44* (42), 23762–23774. DOI: 10.1016/j.ijhydene.2019.07.084.
(20) Polian, A.; Vo-Thanh, D.; Richet, P. Elastic properties of a-SiO_2 up to 2300 K from Brillouin scattering measurements. *Europhysics Letters (EPL)* **2002**, *57* (3), 375–381. DOI: 10.1209/epl/i2002-00470-4.
(21) Kundu, S.; Simon, L. C.; Fowler, M.; Grot, S. Mechanical properties of Nafion™ electrolyte membranes under hydrated conditions. *Polymer* **2005**, *46* (25), 11707–11715.
(22) Dondapati, J. S.; Cohen, L. A.; Stinson, W. D. H.; Jin, J.; Mahajan, S.; Puma, A. M.; Hu, A. K.; Harris, S.; Dameron, A. A.; Weimer, M. S.; et al. Nanoscopic Plugs Block Hydrogen Crossover in Submicron Thick Proton-Conducting SiO_2 Membranes for Water Electrolysis. *ACS Nano* **2025**, *19* (44), 38284–38296. DOI: 10.1021/acsnano.5c09555.
(23) Bhusari, D.; Li, J.; Jayachandran, P. J.; Moore, C.; Kohl, P. A. Development of P-Doped SiO_2 as Proton Exchange Membrane for Microfuel Cells. *Electrochemical and Solid-State Letters* **2005**, *8* (11), A588. DOI: 10.1149/1.2050587.
(24) Kim, H.; Prakash, S.; Mustain, W. E.; Kohl, P. A. Sol–gel based sulfonic acid-functionalized silica proton conductive membrane. *Journal of Power Sources* **2009**, *193* (2), 562–569. DOI: 10.1016/j.jpowsour.2009.04.040.
(25) George, S. M. Atomic Layer Deposition: An Overview. *Chemical Reviews* **2010**, *110* (1), 111–131. DOI: 10.1021/cr900056b.
(26) Klaus, J. W.; Sneh, O.; George, S. M. Growth of SiO_2 at Room Temperature with the Use of Catalyzed Sequential Half-Reactions. *Science* **1997**, *278* (5345), 1934–1936. DOI: 10.1126/science.278.5345.1934.
(27) Mameli, A.; Merkx, M. J. M.; Karasulu, B.; Roozeboom, F.; Kessels, W. M. M.; Mackus, A. J. M. Area-Selective Atomic Layer Deposition of SiO_2 Using Acetylacetone as a Chemoselective

Inhibitor in an ABC-Type Cycle. *ACS Nano* **2017**, *11* (9), 9303–9311. DOI: 10.1021/acsnano.7b04701.
(28) Wagner, C. D.; Passoja, D. E.; Hillery, H. F.; Kinisky, T. G.; Six, H. A.; Jansen, W. T.; Taylor, J. A. Auger and photoelectron line energy relationships in aluminum–oxygen and silicon–oxygen compounds. *Journal of Vacuum Science and Technology* **1982**, *21* (4), 933–944. DOI: 10.1116/1.571870.
(29) Tian, R.; Seitz, O.; Li, M.; Hu, W.; Chabal, Y. J.; Gao, J. Infrared Characterization of Interfacial Si−O Bond Formation on Silanized Flat SiO_2/Si Surfaces. *Langmuir* **2010**, *26* (7), 4563–4566. DOI: 10.1021/la904597c.
(30) Awazu, K.; Kawazoe, H. Strained Si–O–Si bonds in amorphous SiO_2 materials: A family member of active centers in radio, photo, and chemical responses. *Journal of Applied Physics* **2003**, *94* (10), 6243–6262. DOI: 10.1063/1.1618351.
(31) Wang, T.; Jansson, P.; Wildlock, M.; Simic, N.; Cornell, A. Rational design of a membrane-coated cathode for selective electrochemical hydrogen evolution in chlorate electrolysis. *Electrochimica Acta* **2023**, *466*, 143010. DOI: 10.1016/j.electacta.2023.143010.
(32) Zhu, L.-Y.; Li, Y.-C.; Liu, J.; He, J.; Wang, L.-Y.; Lei, J.-D. Recent developments in high-performance Nafion membranes for hydrogen fuel cells applications. *Petroleum Science* **2022**, *19* (3), 1371–1381. DOI: 10.1016/j.petsci.2021.11.004.
(33) Zawodzinski, T. A.; Gottesfeld, S.; Shoichet, S.; McCarthy, T. J. The contact angle between water and the surface of perfluorosulphonic acid membranes. *Journal of Applied Electrochemistry* **1993**, *23* (1), 86–88. DOI: 10.1007/bf00241582.
(34) Dimitrova, P.; Friedrich, K. A.; Vogt, B.; Stimming, U. Transport properties of ionomer composite membranes for direct methanol fuel cells. *Journal of Electroanalytical Chemistry* **2002**, *532* (1-2), 75–83. DOI: 10.1016/s0022-0728(02)01006-9.
(35) Halim, J.; Büchi, F. N.; Haas, O.; Stamm, M.; Scherer, G. G. Characterization of perfluorosulfonic acid membranes by conductivity measurements and small-angle x-ray scattering. *Electrochimica Acta* **1994**, *39* (8-9), 1303–1307. DOI: 10.1016/0013-4686(94)e0051-z.
(36) Meng, X.; Wang, H.-N.; Song, S.-Y.; Zhang, H.-J. Proton-conducting crystalline porous materials. *Chemical Society Reviews* **2017**, *46* (2), 464–480. DOI: 10.1039/c6cs00528d.
(37) Cao, J.; Su, C.; Ji, Y.; Yang, G.; Shao, Z. Recent advances and perspectives of fluorite and perovskite-based dual-ion conducting solid oxide fuel cells. *Journal of Energy Chemistry* **2021**, *57*, 406–427. DOI: 10.1016/j.jechem.2020.09.010.
(38) Nogami, M.; Kato, A.; Nakayama, M.; Lakshminarayana, G. Proton conduction in ionic liquid-modified P_2O_5-SiO_2 glasses. *Journal of Non-Crystalline Solids* **2012**, *358* (24), 3495–3500. DOI: 10.1016/j.jnoncrysol.2012.04.001.
(39) Bhusari, D.; Li, J.; Jayachandran, P. J.; Moore, C.; Kohl, P. A. Development of P-doped SiO_2 as proton exchange membrane for microfuel cells. *Electrochem Solid St* **2005**, *8* (11), A588–A591. DOI: 10.1149/1.2050587.
(40) Namazi, H.; Ahmadi, H. Improving the proton conductivity and water uptake of polybenzimidazole-based proton exchange nanocomposite membranes with TiO_2 and SiO_2 nanoparticles chemically modified surfaces. *Journal of Power Sources* **2011**, *196* (5), 2573–2583. DOI: 10.1016/j.jpowsour.2010.10.082.
(41) Yin, Y. H.; Liu, Y. C.; Wu, H.; Cao, L.; He, X. Y.; Zhang, B.; Wang, C. B.; Jiang, Z. Y. One-pot synthesis of silica-titania binary nanoparticles with acid-base pairs via biomimetic mineralization to fabricate highly proton-conductive membranes. *Journal of Materials Chemistry A* **2017**, *5* (35), 18585–18593. DOI: 10.1039/c7ta03513f.

(42) Hoang, N. D.; Chung, P. S. Hydration-Driven Proton Transport in Speek Membranes: A Coarse-Grained Molecular Dynamics and Experimental Study. *Available at SSRN 5182953*.
(43) Mauritz, K. A.; Moore, R. B. State of understanding of nafion. *Chem Rev* **2004**, *104* (10), 4535–4585. DOI: 10.1021/cr0207123.
(44) Kreuer, K. D. Proton-conducting oxides. *Annual Review of Materials Research* **2003**, *33* (1), 333–359. DOI: 10.1146/annurev.matsci.33.022802.091825.
(45) Frei, H.; Esposito, D. V. *Ultrathin Oxide Layers for Solar and Electrocatalytic Systems*; Royal Society of Chemistry, 2022.
(46) Labrador, N. Y.; Songcuan, E. L.; De Silva, C.; Chen, H.; Kurdziel, S. J.; Ramachandran, R. K.; Detavernier, C.; Esposito, D. V. Hydrogen Evolution at the Buried Interface between Pt Thin Films and Silicon Oxide Nanomembranes. *Acs Catalysis* **2018**, *8* (3), 1767–1778. DOI: 10.1021/acscatal.7b02668.
(47) Yurova, P. A.; Malakhova, V. R.; Gerasimova, E. V.; Stenina, I. A.; Yaroslavtsev, A. B. Nafion/Surface Modified Ceria Hybrid Membranes for Fuel Cell Application. *Polymers* **2021**, *13* (15), 2513. DOI: 10.3390/polym13152513.
(48) Hiller, D.; Zierold, R.; Bachmann, J.; Alexe, M.; Yang, Y.; Gerlach, J.; Stesmans, A.; Jivanescu, M.; Müller, U.; Vogt, J. Low temperature silicon dioxide by thermal atomic layer deposition: Investigation of material properties. *Journal of Applied Physics* **2010**, *107* (6).
(49) Wang, D.; Liu, J.; Lv, Z.; Tao, H.; Cui, Y.; Wang, H.; Liu, S.; Liu, C.; Wang, N.; Jiang, W.; et al. A simple route to deposit SiO2 film with resistivity >109 Ω·μm. *Materials Letters* **2018**, *211*, 277–280. DOI: 10.1016/j.matlet.2017.10.034.
(50) Srivastava, J. K.; Prasad, M.; Wagner, J. B. Electrical-Conductivity of Silicon Dioxide Thermally Grown on Silicon. *Journal of the Electrochemical Society* **1985**, *132* (4), 955–963. DOI: Doi 10.1149/1.2113993.
(51) Standardization, I. O. f. *Hydrogen Generators Using Water Electrolysis*; 2019.